Emergence of Rashba spin valley state in two-dimensional strained bismuth oxychalcogenides Bi_2O_2Se

Muhammad Darwis Umar, Lalu Dalilul Falihin, Arief Lukmantoro, Harsojo, and Moh. Adhib Ulil Absor*

Department of Physics, Faculty of Mathematics and Natural Sciences, Universitas Gadjah Mada, Sekip Utara BLS 21 Yogyakarta 55186 Indonesia

(Received 19 March 2023; accepted 26 June 2023; published 5 July 2023)

The experimental evidence of the ultrahigh electron mobility and strong spin-orbit coupling in the two-dimensional (2D) layered bismuth-based oxyselenide, Bi_2O_2Se, makes it a potential material for spintronic devices. However, its spin-related properties have not been extensively studied due to the centrosymmetric nature of its crystal structure. By using first-principles density-functional theory calculation, this study reports the emergence of Rashba-spin-valley states in Bi_2O_2Se monolayer (ML). Breaking the crystal inversion symmetry of Bi_2O_2Se ML using an external electric field enables the Rashba-spin-valley formation, causing the appearance of the Rashba-type splitting around the Γ valley and spin-valley coupling at the D valleys located near the middle of $\Gamma - M$ line. In addition to the typical Rashba-type spin textures around the Γ valley, the study also observed in-plane unidirectional spin textures around the D valleys, which is a rare phenomenon in 2D materials. The observed Rashba-spin-valley states are driven by the lowering point group symmetry of the crystal from D_{4h} to C_{4v} enforced by the electric field, as clarified through $\vec{k} \cdot \vec{p}$ model derived from symmetry analysis. More importantly, tuning the Rashba and spin-valley states by using biaxial strain offers a promising route to regulate the spin textures and spin splitting preventing the electron from back-scattering in spin transport. Finally, we proposed a more realistic system, namely, Bi_2O_2Se ML/$SrTiO_3$ (001) heterointerface that supports the strong Rashba-spin-valley states and highlighting the potential of the Bi_2O_2Se ML for future spintronics and valleytronics-based devices.

DOI: 10.1103/PhysRevB.108.035109

I. INTRODUCTION

The correlation between the electron spin and orbital degrees of freedom is a fundamental concept in a range of emerging areas, such as spintronics and valleytronics [1–3]. The examination of the symmetry of crystalline solids is critical in comprehending the physical properties of these new fields. For an instant, in a system that possesses both inversion and time-reversal symmetry, the doubly degenerate electronic bands are preserved throughout the first Brillouin zone (FBZ) even in the presence of the spin-orbit coupling (SOC), known as Kramer's spin degeneracy. When the inversion symmetry is broken, the SOC induces the momentum-dependent spin–orbit field (SOF) and lifts the band degeneracy through the so-called Rashba [4] and Dresselhaus [5] effects. During the past decade, the Rashba-Dresselhaus effect has been the subject of intense research due to its potential applications in the emergent field of spintronics [6,7]. In particular, the Rashba effect can manipulate the polarized spins by the external electric field [8] and thus holds promise for realizing spin field effect transistors in experiments [9].

In addition, an intriguing phenomenon arises when the time-reversal symmetry of crystalline solids is broken. In such cases, the absence of inversion symmetry, combined with the SOC, gives rise to the spin-valley contrasting effect [2,10]. Typically, the term valley refers to the energy extrema points in momentum space that represents a binary index for low-energy carriers, which is robust to the scattering by smooth deformations and long-wavelength phonons [10,11]. The valley degree of freedom is potentially utilized to store and carry information, leading to conceptual electronic applications known as valleytronics [12,13]. Moreover, utilization of the spin-valley contrasting effect gives rise to topological valley transport properties such as photoinduced charge Hall effect, valley Hall effect, and spin Hall effect under zero magnetic field [10,14,15]. Several promising systems for hosting the spin-valley contrasting effect have been reported in two-dimensional (2D) systems, including the family of transition metal dichalcogenides (TMDCs) MX_2 (M = W, Mo; X = S, Se, Te) monolayer (ML) [10,14,15] and a class of septuple-atomic-layer MXenes MA_2Z_4 (M = W, Mo; A = Si, Ge; Z = N, P, As Te) ML [16–18]. Here, D_{3h} symmetry of the TMDCs monolayer (ML) enforces the occurrence of the large spin splitting located at the K valley in the FBZ, exhibiting valley-contrasting spin polarization perpendicular to the 2D plane. This effect has been evidenced by its unique optical and transport characteristics, including valley-dependent circular dichroic photoluminescence [19,20] and nonreciprocal charge transport [21].

In some systems with multiple well-separated valleys, the Rashba and spin-valley effects can both be observed. In such cases, coupling between the Rashba and spin-valley states can occur, resulting in Rashba-flavored spin-valley states. These states enable nondissipative transport of both spin and valley degrees of freedom by utilizing the position of the

*Corresponding author: adib@ugm.ac.id

Rashba and spin-valley states near the Fermi level. Typically, Rashba states produce a pair of spin-polarized bands in k space with opposite chiral in-plane spin textures, which allows electrons to backscatter and greatly reduces the efficiency of spin transport [22,23]. In contrast, backscattering is suppressed in spin-valley states due to their unidirectional out-of-plane spin textures [24,25]. The Rashba-spin-valley states have been observed in various 2D ML structures with in-plane mirror symmetry breaking, such as Janus TMDCs MXY (M = W, Mo; X, Y = S, Se, Te) ML [26–28], Janus MXenes $MAA'Z_2Z_2'$ (M = W, Mo; A, A' = Si, Ge; Z, Z' = N, P, As Te) ML [29,30], Janus titanium dihalide TiXY (X, Y = Cl, Br, I) ML [31] and buckled hexagonal h-MN (M = V, Nb, and Ta) ML [32]. However, the close energy proximity between the Rashba and spin-valley states in these systems may induce interference between in-plane and out-of-plane spin textures, resulting in low efficiency of spin transport. Recently, it has been reported that 2D layered centrosymmetric black arsenic also hosts Rashba-spin valley states that can be controlled by electrostatic gating [33]. However, the light atomic weight of arsenic leads to a small spin splitting of the Rashba-spin valley states.

This study utilizes first-principles density-functional theory (DFT) calculations to show that the Rashba-spin-valley states emerge in 2D bismuth oxyselenide, Bi_2O_2Se. Recently, 2D ultrathin layered Bi_2O_2Se has been successfully synthesized, exhibiting the strong SOC interaction [34,35] and superior transport properties such as ultrahigh Hall electron mobility [36–39], making the achievement of Rashba-spin-valley states in this material significant for the development of spintronics and valleytronics applications. We find that breaking the crystal inversion symmetry of 2D Bi_2O_2Se ML using an external electric field leads to the Rashba-spin-valley formation exhibiting the Rashba-types splitting around the Γ valley and spin-valley coupling at D valleys located near the middle of the $\Gamma - M$ line. Unlike previous studies, unidirectional in-plane spin textures around the D valleys are observed, in addition to conventional Rashba-type spin textures around the Γ valley. These spin textures are driven by the electric field-induced lowering of crystal symmetry from D_{4h} to C_{4v} point group, as demonstrated through the $\vec{k} \cdot \vec{p}$ model derived from symmetry analysis. More interestingly, manipulating the Rashba and spin-valley states through biaxial strain offers an efficient means of managing the spin textures and spin splitting, thereby hindering electron backscattering in spin transport. We further propose a more realistic system, namely, Bi_2O_2Se ML/$SrTiO_3$ (001) heterointerface, where the strong Rashba-spin-valley states are achieved. Since molecular beam epitaxy (MBE) of atomically thin Bi_2O_2Se film down to the ML structure grown on the $SrTiO_3$ (001) substrate has been experimentally reported [40], observation of the Rashba effect on the Bi_2O_2Se ML/$SrTiO_3$ (001) is expected to be realized in the near future. Therefore, the application of Bi_2O_2Se ML for spintronics and valleytronics devices is plausible.

II. MODEL AND COMPUTATIONAL DETAILS

To evaluate the structural, electronic, and spin-splitting-related properties of Bi_2O_2Se ML, we performed fully relativistic DFT calculations, where the SOC was taken into account self-consistently by using total momentum (j)-dependent pseudopotentials [41]. We used normconserving pseudopotentials and optimized pseudoatomic localized basis functions in our DFT calculations implemented in the OpenMX code [42–44]. We apply the generalized gradient approximation of Perdew, Burke, and Ernzerhof (GGA-PBE) [45,46] as an exchange-correlation functional. The linear combinations of multiple pseudoatomic orbitals (PAOs) generated using a confinement scheme were used as the basis functions [42–44]. A set of the PAOs basis functions was specified as Bi8.0-$s3p2d2f1$, Sr7.0-$s3p2d2f1$, Ti7.0-$s3p2d2$, Se7.0-$s3p2d2$, O6.0-$s2p2d2$, and H6.0-$s2p2$, where 8.0, 7.0, 7.0, 7.0, 6.0, and 6.0 are the cutoff radii (in bohrs) of Bi, Sr, Ti, Se, O, and H atoms, respectively. Here, the integers after s, p, d, and f indicate the radial multiplicity of each angular momentum component. The accuracy of the basis functions, as well as pseudo-potentials we used, were carefully benchmarked by the delta gauge method [47]. We make a periodic slab model with a sufficiently large vacuum layer (25 Å) to avoid interaction between adjacent layers. We used an $8 \times 8 \times 1$ k point and real space grids corresponding to energy cutoffs larger than 350 Ry to obtain the converged results of the self-consistent field (SCF) loops. The energy convergence criterion of 10^{-9} eV was used. Phonon dispersion band is used to evaluate the dynamical stability of the Bi_2O_2Se ML obtained by using ALAMODE code [48] based on the force constants obtained from the OpenMX code calculations.

To provide a more realistic system, we built a heterostructure where a $SrTiO_3$ [001] substrate is applied on Bi_2O_2Se ML. Here, $SrTiO_3$ [001] surface was modeled using an eight layer slab. Two stable formations of the Bi_2O_2Se ML/$SrTiO_3$ [001] interface are considered, i.e., (i) Se-SrO and (ii) Se-TiO_2 interface termination. The stability of the Bi_2O_2Se ML/$SrTiO_3$ [001] interface was evaluated by calculating the cohesive energy (E_{coh}) through the following relation:

$$E_{\mathrm{coh}} = \frac{E_{\mathrm{Bi_2O_2Se}} + E_{\mathrm{SrTiO_3}} - E_{\mathrm{Tot}}}{A}, \tag{1}$$

where E_{Tot}, $E_{\mathrm{Bi_2O_2Se}}$, and $E_{\mathrm{SrTiO_3}}$ are the total energy of Bi_2O_2Se ML/$SrTiO_3$ [001], Bi_2O_2Se ML surface, and isolate $SrTiO_3$ [001] surface, respectively, while A represents the surface area.

To study the Rashba-spin valley effect, we applied a uniform external electric field on Bi_2O_2Se ML along the z direction modeled by a sawtooth waveform during the SCF calculation and geometry optimization. We calculated the spin textures in the momentum k space by deducing the spin vector components (S_x, S_y, S_z) in the reciprocal lattice vector $\vec{k}$ from the spin density matrix. By using the spinor Bloch wave function, $\Psi_\mu^\sigma(\vec{r}, \vec{k})$, obtained from the DFT calculations after the SCF is achieved, we calculate the spin density matrix, $P_{\sigma\sigma'}(\vec{k}, \mu)$, by using the following equation [49,50]:

$$\begin{aligned} P_{\sigma\sigma'}(\vec{k}, \mu) &= \int \Psi_\mu^\sigma(\vec{r}, \vec{k}) \Psi_\mu^{\sigma'}(\vec{r}, \vec{k}) d\vec{r} \\ &= \sum_n \sum_{i,j} [c^*_{\sigma\mu i} c_{\sigma'\mu j} S_{i,j}] e^{i\vec{R}_n \cdot \vec{k}}, \end{aligned} \tag{2}$$

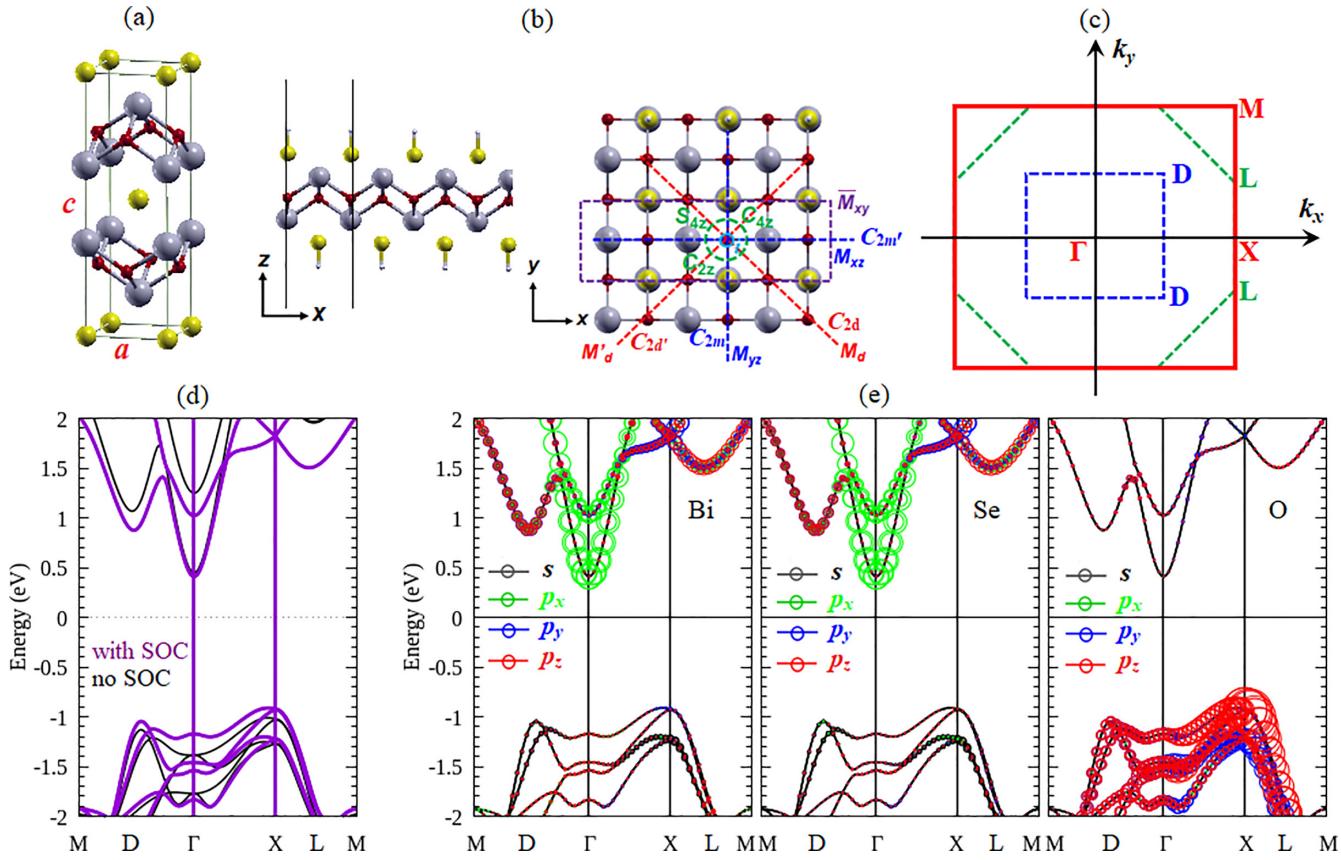

FIG. 1. Atomic structures of Bi_2O_2Se for (a) bulk and (b) monolayer (ML) structures. For the case of the Bi_2O_2Se ML, hydrogen H-passivated configuration is applied for the upper and bottom surface Bi_2O_2Se ML to balance nonstoichiometry. The grey, yellow, red, and white colors represent the Bi, Se, O, and H atoms, respectively. The symmetry operations of the Bi_2O_2Se ML, including E, i, C_{2z}, $C_{2d,d'}$, $C_{2m,m'}$, $C_{4z\pm}$, $S_{4z\pm}$, $\overline{M}_{xy}$, $M_{xz,yz}$, and $M_{d,d'}$ are indicated. (c) 2D FBZ for both the Bi_2O_2Se ML characterized by time-reversal-symmetry points, such as M, Γ, and X points, and non-time-reversal-symmetry points, including D and L points, are highlighted. (d) electronic band structure of Bi_2O_2Se ML calculated without (black color) and with (magenta color) spin-orbit coupling (SOC). (e) Orbital-resolved projected bands for Bi, Se, and O atoms calculated with SOC are shown. The radii of the circles reflect the magnitudes of the spectral weight of the particular orbitals to the bands.

where S_{ij} is the overlap integral of the ith and jth localized orbitals, $c_{\sigma\mu i(j)}$ is the expansion coefficient, σ (σ') is the spin index (↑ or ↓), μ is the band index, and $\vec{R}_n$ is the nth lattice vector. This method has been successfully applied in our recent studies on various 2D materials [51–56].

III. RESULTS AND DISCUSSION

First, we examine the structural properties of Bi_2O_2Se ML. The geometry of the bulk and 2D ML structures are shown in Figs. 1(a)–1(b), while the corresponding 2D FBZ is illustrated in Fig. 1(c). The layered Bi_2O_2Se crystallizes in a tetragonal structure with $I4/mmm$ space group [Fig. 1(a)], consisted of alternating stacking of positively charged $[Bi_2O_2]_n^{2n+}$ layers and negatively charged $[Se_2]_n^{2n-}$ layers with weak electrostatic interactions [36]. The 2D ML structure of Bi_2O_2Se can be constructed by separating the crystal in the c direction (z direction) through the ionic bonds between $[Bi_2O_2]^{2+}$ and Se^{2-} layers [Fig. 1(b)]. Here, the Se^{2-} layers terminate both the top and bottom surface MLs, thus preserving the inversion symmetry. Similar to its bulk counterpart, Bi_2O_2Se ML belongs to the D_{4h} point group symmetry [36,57], generated by the following symmetry operations: E, i, C_{2z}, $C_{2d,d'}$, $C_{2m,m'}$, $C_{4z\pm}$, $S_{4z\pm}$, $\overline{M}_{xy}$, $M_{xz,yz}$, and $M_{d,d'}$. Here, E is the identity operator, i is the inversion symmetry, C_{2z} and $C_{4z\pm}$ represent the twofold and fourfold rotations around the z axis, respectively, $C_{2d,d'}$ and $C_{2m,m'}$ are the twofold rotations around the dihedral and vertical mirror axis, respectively, $S_{4z\pm}$ is the fourfold rotations around the z axis followed by reflection through the xy plane, $\overline{M}_{xy}$ is the glide mirror symmetry through the xy mirror plane followed by translation, $M_{xz,yz}$ is the vertical mirror symmetry through the xz and yz mirror plane, respectively, and $M_{d,d'}$ are the dihedral mirror symmetry containing the z axis and crossing the angle between k_x and $\pm k_y$ [Fig. 1(b)]. In our model, we applied hydrogen H-passivated configuration on Bi_2O_2Se ML for balancing the nonstoichiometry as used in the previous studies [58–61]. We find that this structural configuration is dynamically stable as confirmed by phonon dispersion bands shown in Fig. S1 in the Supplemental Material (SM) [62]. Nevertheless, the optimized in-plane lattice parameter of the ML (3.98 Å) is a bit larger than that of the bulk (3.91 Å), which agrees with prior findings [58–61].

Figure 1(d) depicts the electronic band structure of Bi_2O_2Se ML calculated with and without SOC. It demon-

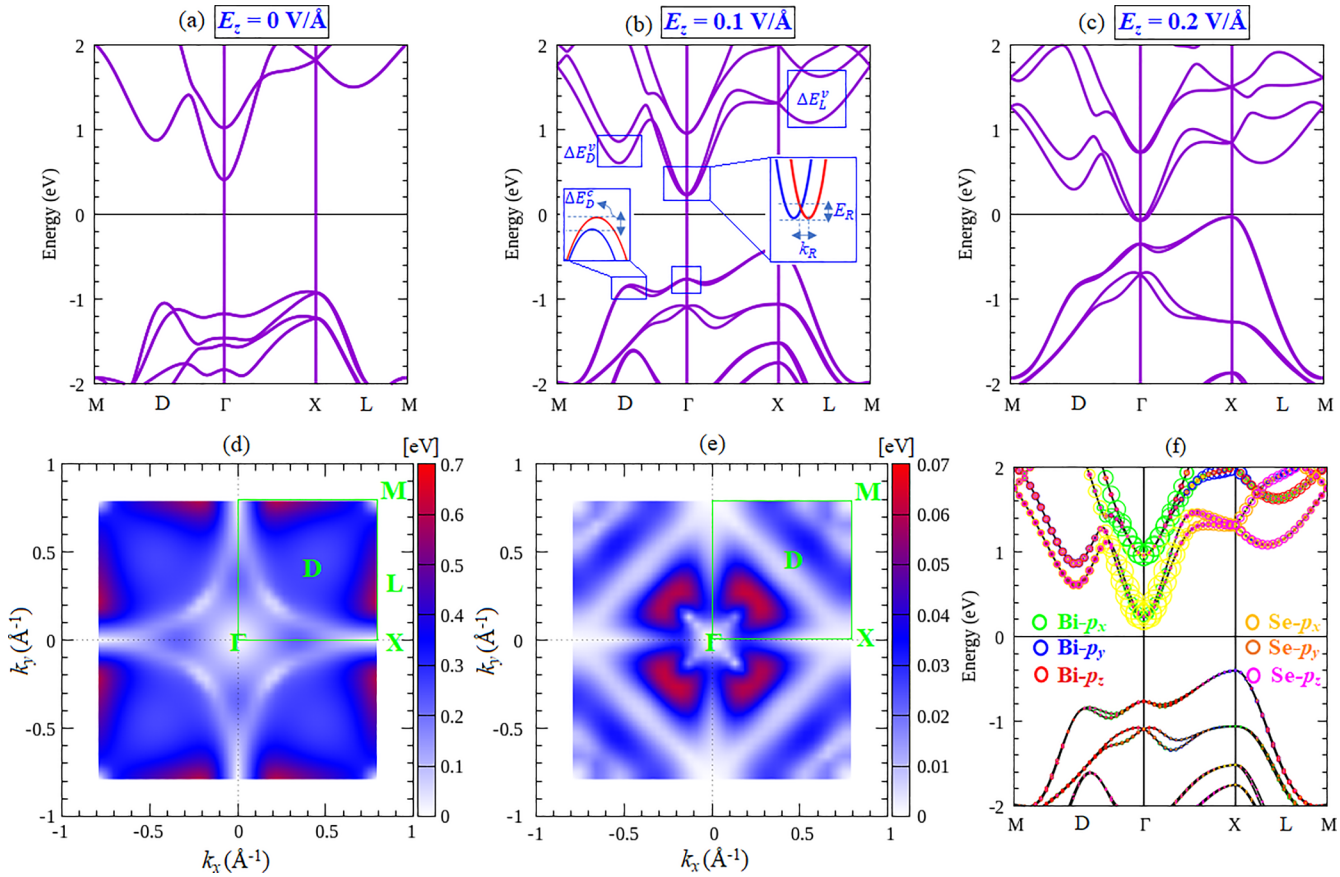

FIG. 2. Evolution of the electronic band structure of Bi_2O_2Se ML calculated with the SOC under the out-of-plane electric field E_z: (a) 0 V/Å, (b) 0.1 V/Å, and (c) 0.2 V/Å. Here, the spin-spin splittings at D, Γ, and L valleys are highlighted. Spin-splitting energy of Bi_2O_2Se ML under E_z of 0.1 V/Å mapped on the first Brillouin zone calculated for (d) CBM and (e) VBM. The spin-splitting energy, $\Delta E(k)$, is calculated by using two bands at the CBM and VBM through the relation, $\Delta E(k) = \|E(k,\uparrow) - E(k,\downarrow)\|$, where $E(k,\uparrow)$ and $E(k,\downarrow)$ are the upper and lower bands of the spin-split states, respectively. (f) Orbital-resolved projected bands near the Fermi level for Bi and Se atoms are shown. The radii of the circles reflect the magnitudes of the spectral weight of the particular orbitals to the bands.

strates that the ML is a semiconductor having multiple valleys in its electronic band structures. Three valleys are observed at the conduction band, with the Γ valley having the lowest energy, the D valley located at the middle of the $\Gamma - M$ line, and the L valley near the middle of the $X - M$ line [Fig. 1(d)]. On the contrary, the valence band is characterized by the D, Γ, and X valleys, with the highest energy level located at the X valleys. The Γ valley in the conduction band mainly comes from the p_x orbitals of the Bi and Se atoms, while the D and L valleys mostly originate from the mixing between $p_{x,y}$ and p_z orbitals of the Bi and Se atoms [Fig. 1(e)]. On the contrary, p_z orbital of the O atoms contributes dominantly to the X, Γ, and D valley at the valence band. Since the conduction band minimum (CBM) and valence band maximum (VBM) is located at the Γ and X valleys, respectively, an indirect band gap is observed. The calculated value of the indirect band gap is 1.2 eV, which is in good agreement with previous theoretical reports [58,60]. We noted here that the indirect band gap of the 2D ultrathin Bi_2O_2Se has been previously reported experimentally by using optical measurement [36]. Although this indirect band gap is well consistent with our calculations, the magnitude of the experimental band gap (1.95 eV) [36] is larger than that of our result (1.2 eV), which is due to the use of the GGA-PBE in our DFT calculations. However, the topological band curvature including the position of the CBM and VBM obtained in our calculations is consistent-well with the angle-resolved photoemission spectroscopy experiment [36,38]. When the SOC is taken into account, the indirect band gap of Bi_2O_2Se ML decreases to 1.1 eV. Since the inversion symmetry is preserved in Bi_2O_2Se ML, all the bands are spin degenerated [see red line in Fig. 1(d)]. Thus, there is no spin-splitting observed on Bi_2O_2Se ML.

In order to observe spin splitting in a Bi_2O_2Se ML, an external electric field (E_z) perpendicular to the ML surface is employed to break the crystal inversion symmetry. We utilized electric fields E_z reaching a magnitude of 0.2 V/Å, demonstrating thermodynamic stability as confirmed by the absence of imaginary frequency in the phonon dispersion; see Figs. S1 in the SM [62]. Figures 2(a) and 2(c) illustrate evolution of the band structures of Bi_2O_2Se ML with different magnitudes of E_z, revealing that when E_z is smaller than 0.18 V/Å, the indirect band gap remains, but at larger E_z of 0.18 V/Å, it becomes metallic. This change from an indirect semiconductor to a metallic state, which is similar to that previously reported on InSe ML [63] and bilayer phosphorene [64], is due to the strong coupling between the p-p orbitals of Bi, Se, and O atoms in both the CBM and VBM [refer to Fig. 1(e)]. Additionally, the breaking of inversion symmetry together

TABLE I. The spin-splitting parameters of the Rashba-spin-valley states calculated for the CBM [$\Delta E^{c}_{D,L}$ (eV), α^{c}_{R} (eVÅ)] and VBM [ΔE^{v}_{D} (eV), α^{v}_{R} (eVÅ)] of the Bi_2O_2Se ML under the influence of the E_z of 0.1 V/Å compared to those reported on the several 2D systems.

ML systems	$\Delta E^{c,v}_{\text{valley}=D,L,K}$ (eV)	$\alpha^{c,v}_{R}$ (eVÅ)	Reference
Bi_2O_2Se	0.32 (D valley, CBM)	1.33 (CBM)	This work
	0.68 (L valley, CBM)		
	0.11 (D valley, VBM)	0.52 (VBM)	
2D Janus TMDCs MXY			
MoSSe	0.17 (K valley)	0.07	Ref. [26]
WSTe	0.49 (K valley)	0.48	Ref. [27]
WSeTe	0.45 (K valley)	0.92	Ref. [28]
2D Janus MXenes $MAA'Z_2Z'_2$			
Mo(W)$Si_2P_xAs_y$ ($x+y=4$)	0.14–0.51 (K valley)	0.0–0.61	Ref. [29]
Mo(W)$Ge_2P_2As_2$	0.14–0.47 (K valley)	0.5–0.52	Ref. [30]
2D Janus TiXY (X, Y = Cl, Br, I)	0.04–0.06 (K valley)	0.07	Ref. [31]
Other 2D materials			
BAs ML	0.004 (D valley)		Ref. [33]
h-MN (M: V, Nb, Ta)	0.01–0.11 (K valley)	0.55–4.23	Ref. [32]

with SOC generates spin-splitting bands throughout the FBZ, except for high symmetry points at Γ, X, and M valleys, which remain time-reversible [see Figs. 2(b) and 2(c)]. Since the spin splitting is more prominent in the bands near the Fermi level [Figs. 2(b) and 2(c)], hence this paper primarily focuses on the spin-split bands at both the CBM and VBM.

Figures 2(d) and 2(e) depict the spin-splitting energy of a Bi_2O_2Se ML at an E_z of 0.1 V/Å mapped throughout the FBZ and computed at the CBM and VBM, respectively. Our findings reveal that the spin splitting shows a highly isotropic character around the center of the FBZ (Γ valley), whereas it becomes strongly anisotropic near the edge of the FBZ (X and M valleys). More interestingly, it is evident that large spin splittings occur in both the CBM and VBM, which is particularly visible at the D valley ($\Delta E^{c}_{D} = 0.32$ eV; $\Delta E^{v}_{D} = 0.11$ eV) and L valley ($\Delta E^{c}_{L} = 0.68$ eV), and there is also an apparent significant Rashba-type spin splitting around the Γ valley [refer to Figs. 2(b), 2(d) and 2(e)]. Due to time reversibility at the Γ valley, the spin splittings are shown to have opposite signs at the $+D$ ($+L$) and $-D$ ($-L$) valleys, giving rise to an effective coupling between spin and valley pseudospin. In addition, due to the close energy between the Γ and D valleys, the Rashba-spin-valley states are achieved. Our calculations confirmed that the strong coupling between the $p_{x,y}$ and p_z orbitals of Bi and Se atoms is responsible for inducing the substantial spin splitting at the D and L valleys, as evidenced by the orbital-resolved projected spin-split bands shown in Fig. 2(f). On the other hand, the Rashba spin splitting around the Γ valley can be quantified by using the Rashba parameter obtained from the linear Rashba model through the relation, $\alpha_R = 2E_R/k_R$, where E_R and k_R are the Rashba energy and momentum offset, respectively [see the insert of Fig. 2(b)]. Then, we summarize the calculated results of the spin-splitting parameters ($\Delta E^{c,v}_{D}$, ΔE^{c}_{L}, $\alpha^{c,v}_{R}$) in Table I, and compare these results with a few selected 2D materials supported Rashba-spin-valley states. Notably, the spin splittings at the D ($\Delta E^{c,v}_{D}$) and L (ΔE^{c}_{L}) valleys are comparable with that observed in various 2D Janus TMDCs MXY ML [26–28] and Janus MXenes $MAA'Z_2Z'_2$ ML [29,30], while the Rashba parameter $\alpha^{c,v}_{R}$ around the Γ valley is much larger than those 2D Janus systems. Additionally, all of the splitting parameters ($\Delta E^{c,v}_{D}$, ΔE^{c}_{L}, and $\alpha^{c,v}_{R}$) of the Rashba-spin-valley states are significantly larger than those observed on 2D Janus TiXY (X, Y = Cl, Br, I) ML [31], 2D buckled h-MN (M: V, Nb, Ta) ML [32], and 2D BAs ML [33].

To gain a better understanding of the observed spin splitting of the Rashba-spin-valley states, we show in Figs. 3(a)–3(c) expectation value of spin components (S_x, S_y, S_z) projected onto the spin-split bands near the Fermi level. Our findings show that the in-plane spin components (S_x, S_y) are the dominant contributors to the spin-split bands, while the out-of-plane spin components (S_z) make only a negligible contribution. By calculating the energy-dependent spin textures projected onto the FBZ, we observed a typical Rashba spin rotation for the spin textures around the Γ valleys, whereas the spin textures become unidirectional pointing along the direction which is parallel to the $k_x - k_y$ plane around the D valleys [Figs. 3(d) and 3(e)]. In particular, the observed unidirectional in-plane spin textures persistently around the D valley are strongly different from the spin textures of the spin-valley states observed on various 2D valleytronics materials where the fully-out-of plane spin textures are observed around the K valley [10,14–18,26–32]. The observed unidirectional in-plane spin textures in the present system lead to the formation of the persistent spin textures [53–56,65–67], which can prevent the electron from the backscattering in spin transport and induces long-lived helical spin-wave mode through suppressing the Dyakonov spin-relaxation mechanism [22,68,69], which is promising for efficient spintronics.

To clarify the origin of the observed spin splitting of Rashba-spin-valley states, we develop a two $\vec{k}\cdot\vec{p}$ band dispersion model derived from the symmetry analysis. This band dispersion can be determined by identifying all terms allowed by symmetry so that $H(\vec{k}) = O^{\dagger}H(\vec{k})O$, where O represents symmetry operations associated with the wave vector group (G) corresponding to the high-symmetry point and time-reversal symmetry. The invariant Hamiltonian should satisfy

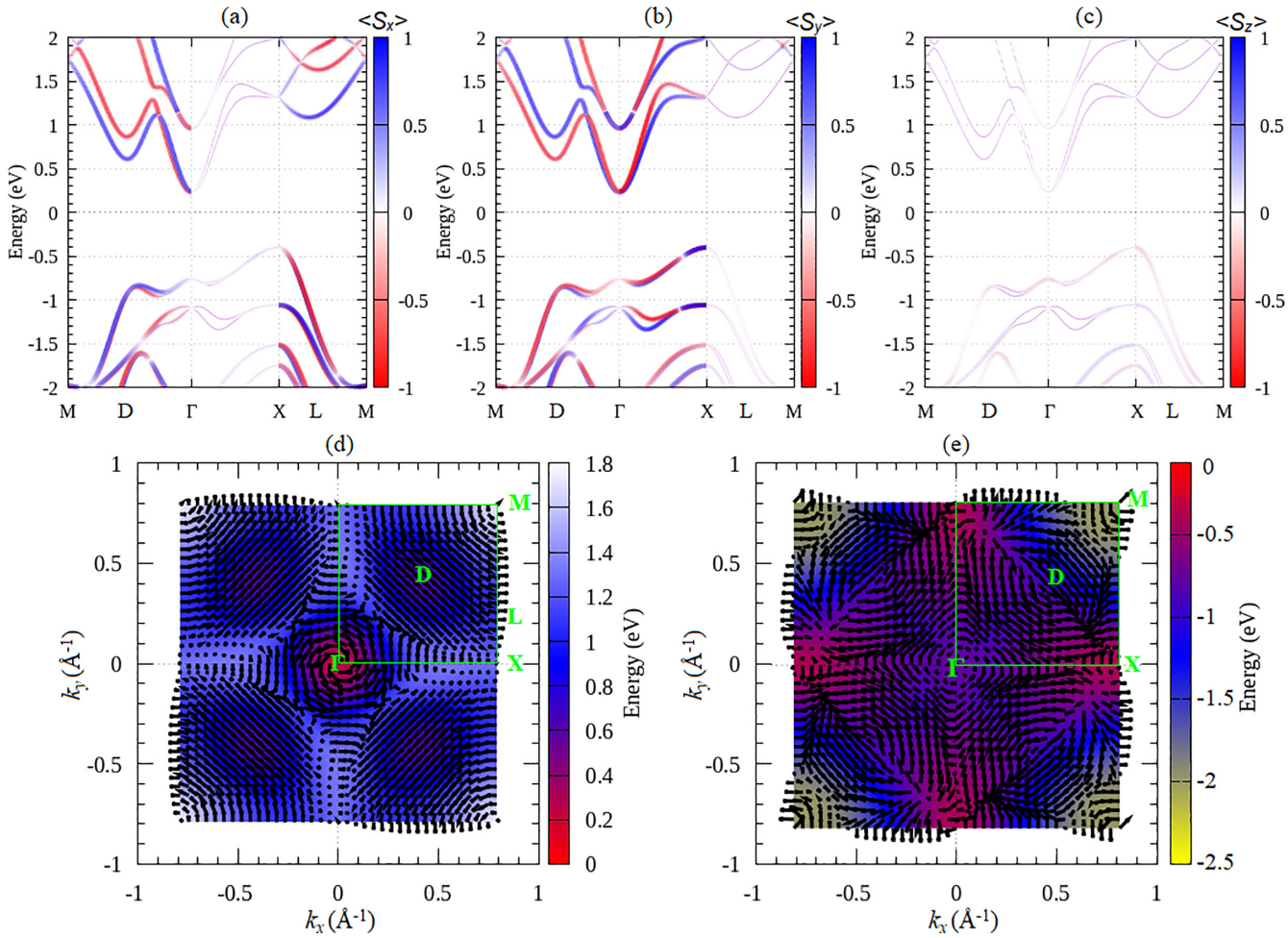

FIG. 3. k-space spin component vector and spin texture of Bi_2O_2Se ML under the electric field E_z of 0.1 V/Å. The expectation value of (a) S_x, (b) S_y, and (c) S_z spin components projected to the spin-split bands near the VBM is shown. (d) and (e) Energy-dependent of spin textures for the upper bands calculated near the CBM and VBM, respectively, are shown.

the condition given below [70]:

$$H_G(\vec{k}) = D(O)H(O^{-1}\vec{k})D^{-1}(O),\ \forall O \in G, T, \qquad (3)$$

where $D(O)$ is the matrix representation of operation O belonging to point group of the wave vector G.

As mentioned previously that Bi_2O_2Se ML belongs to D_{4h} PGS. When the electric field E_z is applied, the symmetry of the crystal reduces to C_{4v} point group, where the following symmetry operations, E, C_{2z}, $C_{4z\pm}$, $M_{xz,yz}$, and $M_{d,d'}$, remain. By using the transformation rules for the wave vector $\vec{k}$ and spin vector $\vec{\sigma}$ given in Table II, the symmetry-allowed SOC Hamiltonian up to third order term is given by

$$H_\Gamma(k) = H_0(k) + \alpha(k_x\sigma_y - k_y\sigma_x) + \alpha' k_x k_y(k_y\sigma_y - k_x\sigma_x) + \alpha''\left(k_x^3\sigma_y - k_y^3\sigma_x\right), \qquad (4)$$

where $H_0(k)$ is the Hamiltonian of the free electrons with eigenvalues $E_0(k) = (\hbar^2 k_x^2/2m_x^*) + (\hbar^2 k_y^2/2m_y^*)$, m_x^* (m_y^*) is effective mass of electron evaluated from the band dispersion along the k_x (k_y) directions, k_i ($i = x, y$) are the components of the wave vector k given regarding the Γ point taken as the origin, and σ_i are the Pauli matrices. Here, α is the Rashba parameter which depends linearly on the electric field, $\alpha \approx |E_z|$. Moreover, the two last terms in Eq. (4) which depend on α' and α'' are the third-order terms in k, and are consistent with the derivation made by Vajna *et al.* [71] and Arras *et al.* [72]. The term $\alpha(k_x\sigma_y - k_y\sigma_x)$ in Eq. (4) has the usual form of the linear Rashba effect, which explains the isotropic in-plane Rashba spin rotation of the spin texture shown in Figs. 3(d) and 3(e). Moreover, near the D valley, we find that $k_x \approx k_y = \tilde{k}$, and we obtain that $H_D = \alpha\tilde{k}(\sigma_y - \sigma_x)$. This

TABLE II. Transformation rules for the wave vector $\vec{k}$ and spin vector $\vec{\sigma}$ under the C_{4v} point-group symmetry.

Symmetry operations	(k_x, k_y)	$(\sigma_x, \sigma_y, \sigma_z)$
E	(k_x, k_y, k_z)	$(\sigma_x, \sigma_y, \sigma_z)$
C_{2z}	$(-k_x, -k_y, k_z)$	$(-\sigma_x, -\sigma_y, \sigma_z)$
C_{4z+}	$(-k_y, k_x, k_z)$	$(-\sigma_y, \sigma_x, \sigma_z)$
C_{4z-}	$(k_y, -k_x, k_z)$	$(\sigma_y, -\sigma_x, \sigma_z)$
M_d	$(-k_y, -k_x, k_z)$	$(\sigma_y, \sigma_x, -\sigma_z)$
$M_{d'}$	(k_y, k_x, k_z)	$(-\sigma_y, -\sigma_x, -\sigma_z)$
M_{xz}	$(k_x, -k_y, k_z)$	$(-\sigma_x, \sigma_y, -\sigma_z)$
M_{yz}	$(-k_x, k_y, k_z)$	$(\sigma_x, -\sigma_y, -\sigma_z)$

shows that the spin texture is unidirectionally oriented in the in-plane direction parallel to the k_x-k_y plane, which is also well consistent with the observed spin textures around the D valley presented in Figs. 3(d) and 3(e).

Solving the eigenvalue problem involving the Hamiltonian of Eq. (4), we obtain the spin-dependent eigenvalues $[E_+(k,\uparrow), E_-(k,\downarrow)]$. Accordingly, the splitting energy of the spin-split bands, $\Delta E(k) = \|E(k,\uparrow) - E(k,\downarrow)\|$, can be evaluated along the $\Gamma - X$ and $\Gamma - M$ lines as follows:

$$\Delta E_{\Gamma-X}(k) = 2\left(\alpha k_x + \alpha'' k_x^3\right) \tag{5}$$

and

$$\Delta E_{\Gamma-M}(k) = 2(\alpha k_\parallel + \widetilde{\alpha} k_\parallel^3), \tag{6}$$

with $k_\parallel = \sqrt{k_x^2 + k_y^2}$ and $\widetilde{\alpha} = \alpha' + \alpha''$. The parameters α and $\widetilde{\alpha}$ can be obtained by numerically fitting Eqs. (5) and (6) to the spin splitting energy along the $\Gamma - X$ and $\Gamma - M$ lines obtained from our DFT calculations, respectively. We find that the calculated α and $\widetilde{\alpha}$ are 1.34 eVÅ(1.33 eVÅ) and 0.003 eVÅ^3 (0.01 eVÅ^3) for the spin-split bands at the CBM along the $\Gamma - X$ ($\Gamma - M$) line, respectively, while they are 0.524 eVÅ(0.517 eVÅ) and 0.01 eVÅ^3 (0.004 eVÅ^3) for the spin-split bands at the VBM along the $\Gamma - X$ ($\Gamma - M$) line, respectively. It is obvious that the obtained value of the cubic term parameters $\widetilde{\alpha}$ in both the $\Gamma - X$ and $\Gamma - M$ lines is too small compared with that of the linear-term parameter α, indicating that the contribution of the higher-order correction is not essential. On the other hand, the calculated values of α which give an almost isotropic linear-Rashba parameter ($\alpha_{\Gamma-X} \approx \alpha_{\Gamma-M}$) obtained from the higher-order correction is fairly agreement with that obtained from the linear Rashba model; see Table I.

Thus far, we have found that the Rashba-spin-valley state is observed in the Bi_2O_2Se ML, which is expected that this ML is suitable for spintronics. However, considering the different features of the spin textures around the Γ and D valleys [Figs. 3(d) and 3(e)], interference of the spin-polarized states may occur, which is not beneficial for spin transport. Although the appearance of the persistent spin textures observed around the D valleys may hold nondissipative spin transport [22,68,69], it may be disturbed by the Rashba spin texture around the Γ valley owing to the backscattering of electrons [22,23]. Therefore, suppressing the position of the Rashba states at the Γ valley to be higher in energy than that of the spin-valley state at D valley enables to prevent of the interference of the spin-polarized states. Since the multiple valleys observed near the band edges (CBM and VBM) are mostly characterized by the p-p coupling orbitals [Fig. 1(e)], the valley positions in the electronic band structures can be effectively modified by the application of the biaxial strain. In fact, the valley-dependent strain has been previously reported on 2D black phosphorene-type structures such as group IV monochalcogenide [73,74]. Therefore, manipulating the Rashba-spin-valley states through biaxial strain offers an efficient route of managing the spin textures and spin splitting, thereby hindering electron back-scattering in spin transport.

We then introduce a wide range of biaxial strain (up to ±10%), which is applied to the in-plane lattice constant of the Bi_2O_2Se ML. We define the degree of in-plane biaxial strain as $\epsilon_{xx} = \epsilon_{yy} = (a - a_0)/a_0 \times 100\%$, where a_0 is the unstrained in-plane lattice constant. Two different biaxial strains are studied, including the tensile strain, which increases the in-plane lattice constant a, and the compressive strain, which decreases a. Our calculated results of the optimized structures revealed that these biaxial strains sustain the crystal symmetry and maintain the dynamical stability of the Bi_2O_2ML as evidenced by the phonon dispersion bands depicted in Fig. S1 of the SM [62]. The strain-dependent of electronic band structures of the Bi_2O_2Se ML under different strain conditions is shown in Fig. 4. Consistent with previous reports [58,60,61], it is revealed that the strained ML remains a semiconductor at large strain up to $\epsilon_{xx} = \pm 10\%$. Under the tensile strain, an indirect band gap from Γ valley (CBM) to X valley (VBM) is similar to that of the equilibrium case. Conversely, the CBM starts to shift from the Γ to D valleys under the compressive strain larger than 4.8%. For the case of $\epsilon_{xx} = -6\%$, the D valley is located much lower in energy than that of the Γ valley at the CBM with a different energy of 0.42 eV. However, at the VBM, it is observed that the energy shift of the D valley exceeds that of the Γ valley by up to 0.23 eV. The decreasing (increasing) energy level of the D valley with respect to the Γ valley in the CBM (VBM) is expected to be useful for the spintronics since the spin texture of the spin-valley state around the D valley could induce the spin-polarized states with minimal interference from the Rashba state around the Γ valley.

To clarify this, we further apply an external electric field E_z of 0.2 V/Å on the Bi_2O_2Se ML with $\epsilon_{xx} = -6\%$ to observe the properties of the spin-polarized states. Concerning the large splitting bands at the CBM [Fig. 5(a)], we confirmed the presence of Rashba spin textures around the Γ valley [Fig. 5(b)] and in-plane persistent spin textures around the D valleys [Fig. 5(c)]. By comparing spin textures calculated at different constant energy cuts of the Fermi line (E_F) presented in Figs. 5(d)–5(f), we clarified the possible interference of the spin-polarized states around the Γ and D valleys. At $E_F = 0.5$ eV, all spin textures had a unidirectional in-plane orientation parallel to the $k_x - k_y$ plane, indicating that the spin-polarized states were achieved without any backscattering. However, at larger E_F [Figs. 5(e) and 5(f)], the mixing of spin textures around the Γ and D valleys resulted in the interference of spin-polarized states. Remarkably, nondissipative spin transport can be achieved by tuning the position of the E_F in the strained Bi_2O_2Se ML, which is important for operating spintronics devices.

Now, we discuss the strain-electric field-dependent of the Γ-D valley positions as well as their spin-splitting energy. Figures 6(a) and 6(b) show the energy difference of the Γ and D valleys with respect to the Fermi level ($\delta^{c,v}_{E_\Gamma - E_D}$) under the different strain and electric field [see the insets of Figs. 6(a) and 6(b) for the schematic view of $\delta^{c,v}_{E_\Gamma - E_D}$]. It is revealed that $\delta^{c,v}_{E_\Gamma - E_D}$ exhibit similar trends in both the CBM and VBM under different strain-electric field conditions. At the CBM, the positive value of $\delta^{c}_{E_\Gamma - E_D}$ is achieved under the compressive biaxial strain started from $\epsilon_{xx} = -4\%$ and increases in magnitude under the increasing of the compressive biaxial strain and electric fields [Fig. 6(a)]. Here, the CBM is mostly occupied by the D valley states. Accordingly, the

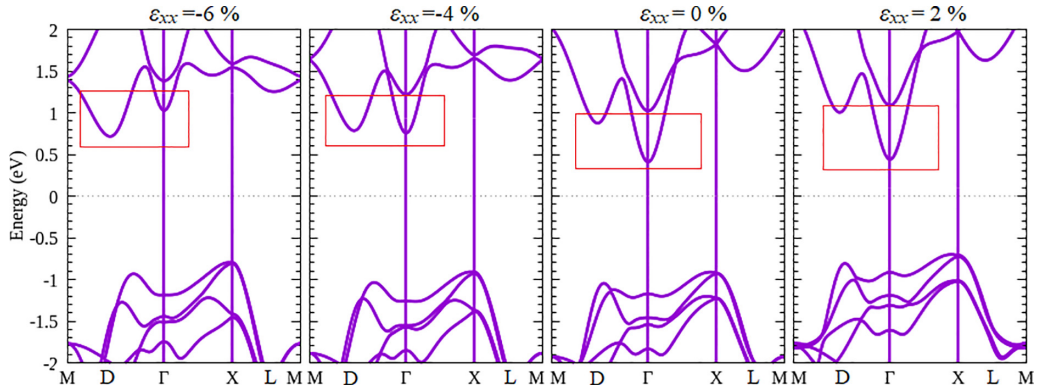

FIG. 4. Strain-dependent of the electronic band structure calculated with the SOC is shown. The shift of the valley position in the CBM is highlighted.

spin-polarized states are driven by the in-plane persistent spin texture suppressing the backscattering of electrons and resulting in a highly efficient spin transport. On the other hand, the value of $\delta^{c}_{E_\Gamma - E_D}$ becomes negative when the tensile strain is applied, making the position of the CBM occupied by the Γ valley state. Therefore, the spin-polarized states experience backscattering due to the presence of the Rashba spin textures around the Γ valley, and hence significantly reduces the efficiency of the spin transport. Since the similar trend of $\delta^{c}_{E_\Gamma - E_D}$ also holds for $\delta^{v}_{E_\Gamma - E_D}$ in the VBM [Fig. 6(b)], the similar character of the spin-polarized states is also expected. Considering the fact that the spin-splitting energy at the *D* valley in both the CBM and VBM is tunable by the strain and electric field [Figs. 6(c) and 6(d)], thus the present systems can be used as a promising platform for spintronic devices.

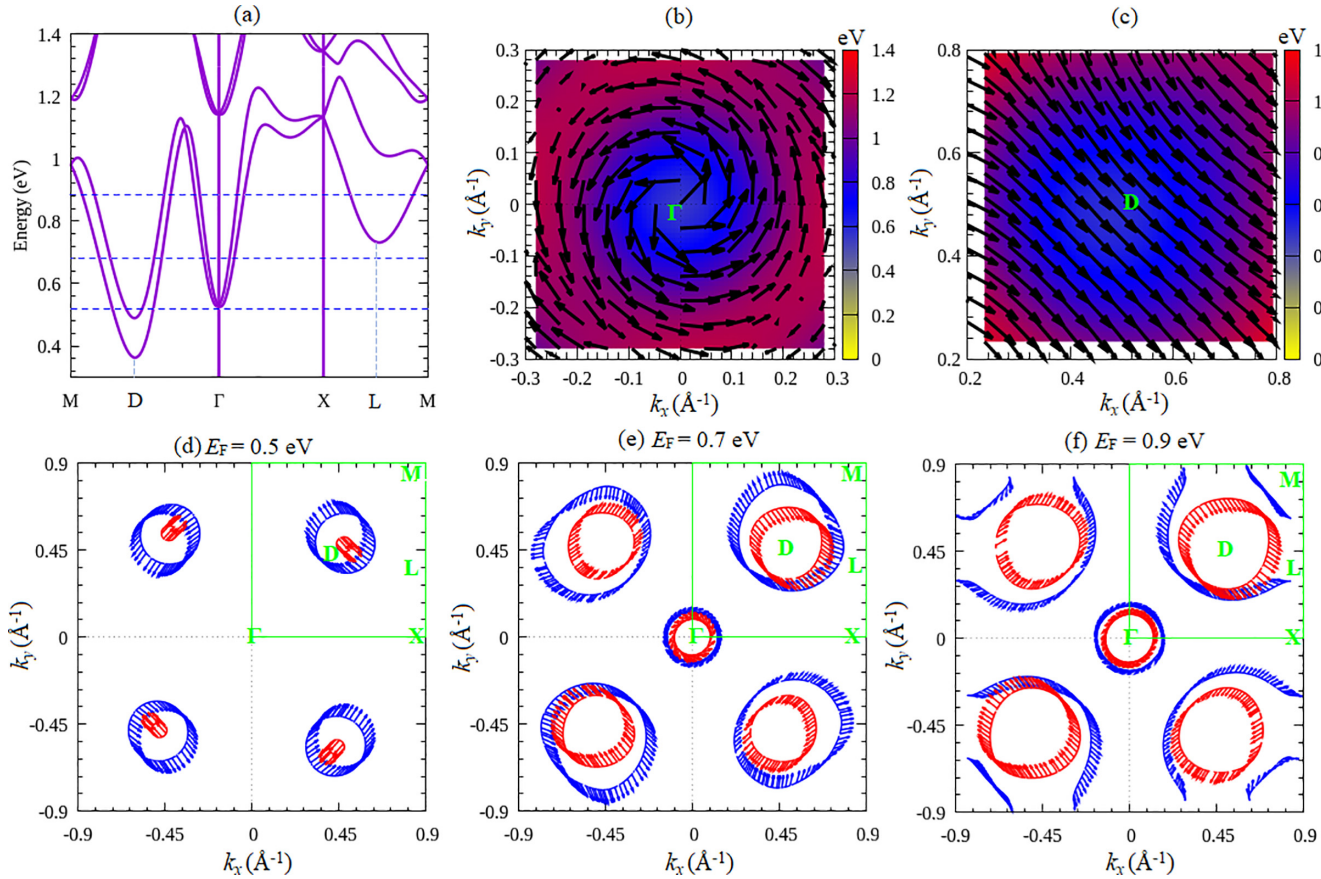

FIG. 5. (a) The spin-split bands of the Bi_2O_2Se ML with $\epsilon_{xx} = -6\%$ under the electric field E_z of 0.2 V/Å is shown. (b) and (c) Energy-dependent of the spin textures for the lower bands calculated around the Γ and *D* valleys near the CBM, respectively, is shown. (d) The spin textures calculated at different constant energy cuts of the Fermi line (E_F) for: (d) $E_F = 0.5$ eV, (e) $E_F = 0.7$ eV, and (f) $E_F = 0.9$ eV, are presented.

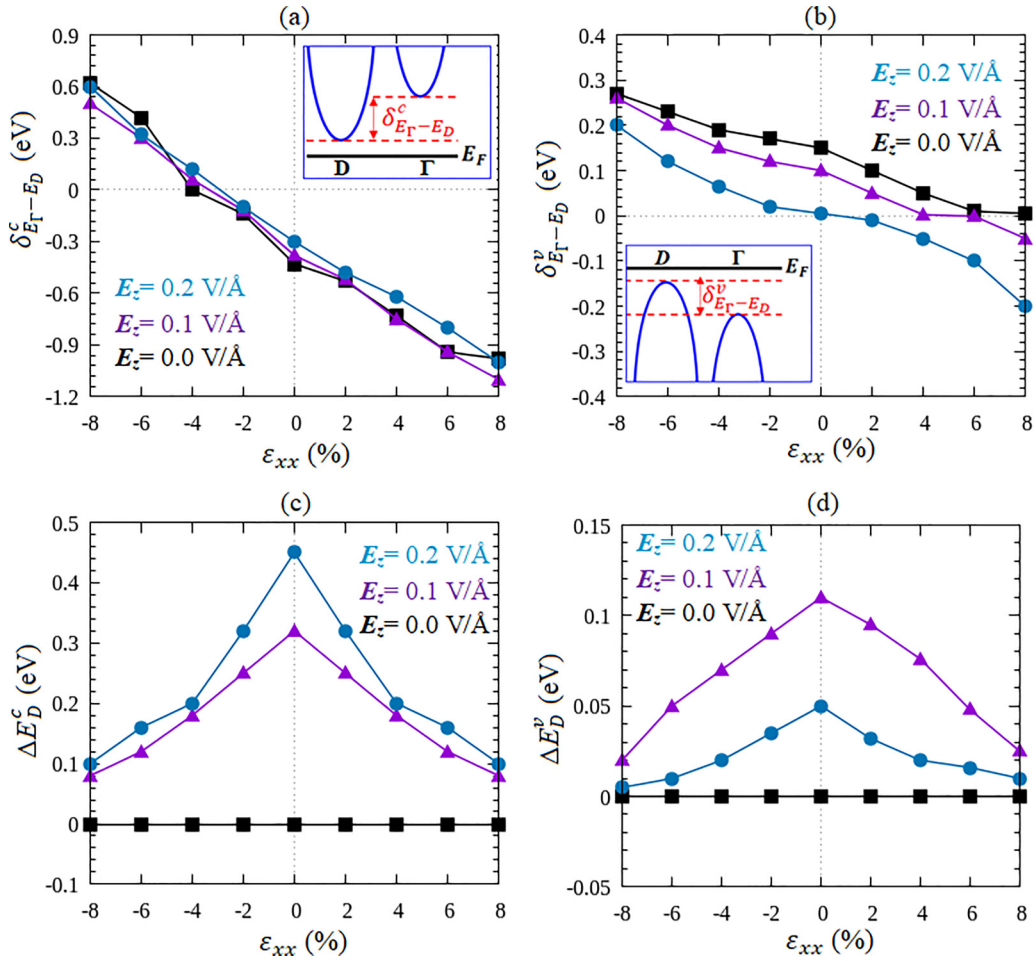

FIG. 6. (a), (b) Energy difference of the Γ and D valleys ($\delta^{c,v}_{E_\Gamma - E_D} = E_\Gamma - E_D$) as a function of biaxial strain for different strength of the external electric field E_z calculated for the CBM and VBM, respectively. The insert shows the schematic view of the energy level of the Γ and D valleys with respect to the Fermi level to define $\delta^{c,v}_{E_\Gamma - E_D}$. (c), (d) Strain-electric field-dependent of the spin-splitting energy at the D valley calculated for the CBM and VBM is shown, respectively.

Finally, we explore the emergence of Rashba-spin-valley states in Bi_2O_2Se ML by considering a more realistic system. In this study, we propose an interfacial configuration consisting of a Bi_2O_2Se ML grown on a $SrTiO_3$ [001] substrate. We investigate two different interface terminations, namely Se-SrO and Se-TiO_2 terminations, as depicted in Fig. 7(a). Both interface systems exhibit positive cohesive energies ($E_{coh}^{Se\text{-}SrO} = 0.06$ eV/Å^2 and $E_{coh}^{Se\text{-}TiO_2} = 0.08$ eV/Å^2), indicating a thermodynamically stable binding between the Bi_2O_2Se ML and $SrTiO_3$. Additional details, including the optimized interfacial lattice constant, interfacial distance, and interfacial charge transfer properties based on the average electrostatic potential, can be found in Table S1 and Fig. S2 in the SM [62]. Overall, our calculations confirm that the interfacial strength and stability of both interface systems are closely related to the bonding characteristics at the heterointerface.

Figures 7(b) and 7(c) show the electronic band structure of Bi_2O_2Se ML/$SrTiO_3$ interface with Se-SrO and Se-TiO_2 interface terminations calculated without (black) and with (red) including the SOC, respectively. Due to the defect contributor of the Bi_2O_2Se ML in the Bi_2O_2Se ML/$SrTiO_3$ interface, several occupied states near the Fermi level are observed, resulting in semimetallic features of the electronic states. We find that the occupied states mainly originated from the Se-p mixing with Bi-6p states of the Bi_2O_2Se, while the unoccupied states are contributed mainly by the Ti-d states with a small admixture of O-2p and Sr-d states of $SrTiO_3$, see Fig. S3 in the SM [62]. Importantly, we identify large spin splitting, which occurs around the D and L valleys as highlighted in Fig. 7(c). The calculated spin-splitting parameters (ΔE_D^{occ}, ΔE_D^{unocc}, ΔE_L^{unocc}, $\alpha_{R,\Gamma}^{occ}$, $\alpha_{R,\Gamma}^{unocc}$) are listed in Table III for different interface terminations. Although these parameters are smaller than that of the Bi_2O_2Se ML, they are still comparable with that reported on various 2D materials listed in Table I. Moreover, these splittings exhibit highly persistent in-plane spin textures around the D valley and the Rashba spin textures around the Γ valley [see Figs. 7(d) and 7(e)], indicating that the Rashba-spin-valley states is achieved similar to that observed on the Bi_2O_2Se ML. Due to a significant energy difference of approximately 0.22 eV between the D valley and the Γ valley in the highest occupied state, the dominance of in-plane persistent spin textures is expected to govern the spin-polarized states. This dominance serves as a protective mechanism against decoherence, facilitating nondissipative spin transport. Given the experimental report by Liang *et al.* [40] on the successful MBE growth of an

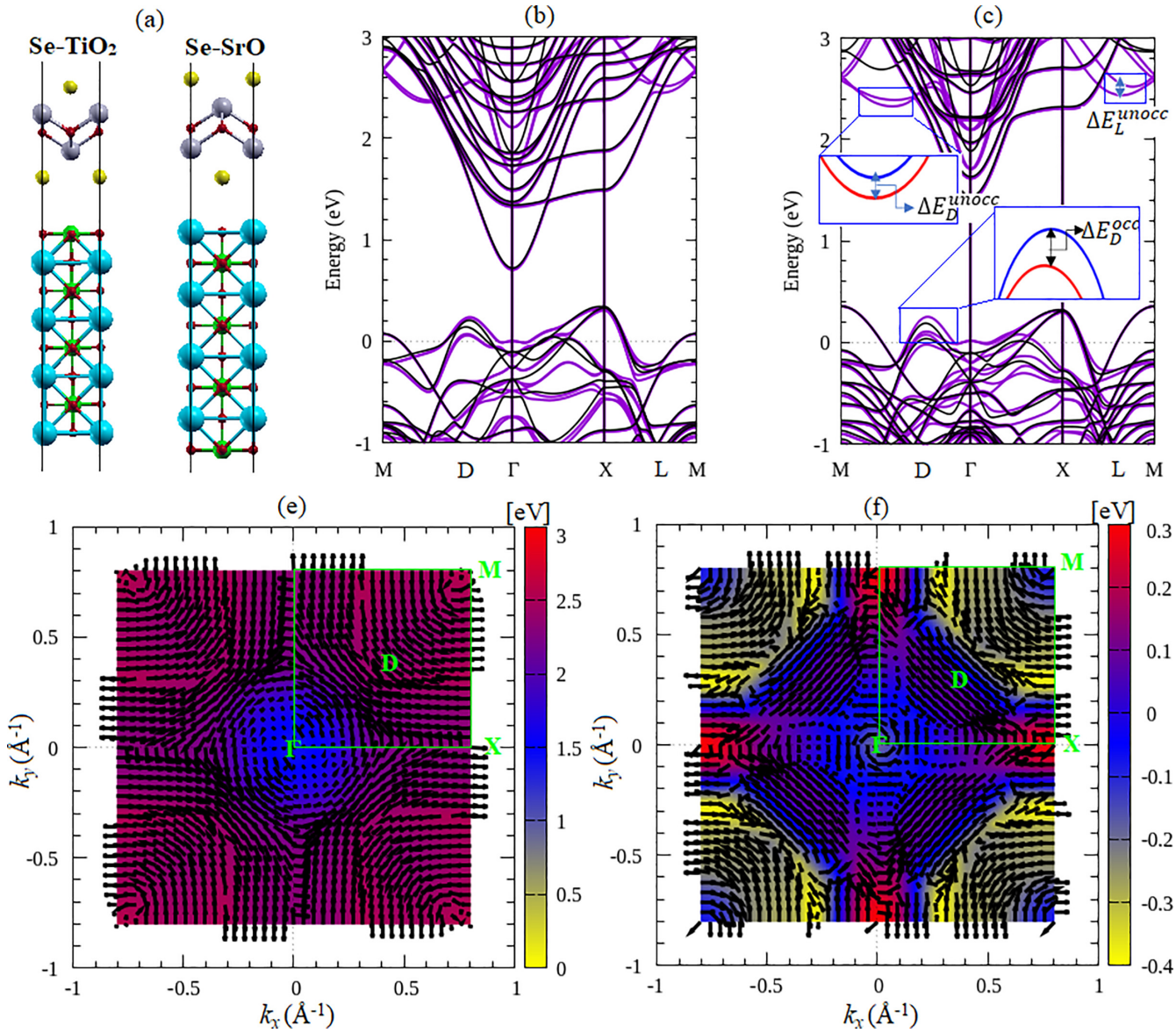

FIG. 7. (a) Atomic structures of Bi_2O_2Se ML/$SrTiO_3$ [001] heterointerface with Se-SrO (left) and Se-TiO_2 (right) interface terminations are shown. The grey, yellow, red, blue, and green colors represent the Bi, Se, O, Sr, and Ti atoms, respectively. The electronic band structures calculated with and without the SOC for Bi_2O_2Se ML/$SrTiO_3$ [001] heterointerface with (b) Se-TiO_2 and (c) Se-SrO interface terminations, are given. The inset in (c) highlights the spin-splitting bands at the highest occupied states around the *D* valley and the lowest unoccupied states around the *D* and *L* valleys. The calculated results of the energy-dependent of the spin textures projected to the FBZ for Bi_2O_2Se ML/$SrTiO_3$ [001] heterointerface with Se-SrO interface terminations calculated for (d) the lowest unoccupied and (e) highest occupied states are shown.

atomically thin Bi_2O_2Se film with an ML structure on the SrTiO3 (001) substrate, it is expected that the observation of the Rashba-spin-valley states in the Bi_2O_2Se ML/$SrTiO_3$ (001) system will soon be achievable.

TABLE III. The spin-splitting energy at *D* and *L* valleys calculated at the highest occupied and lowest unoccupied states for Bi_2O_2Se ML/$SrTiO_3$ interface with different interface terminations is given. ΔE_D^{occ} (eV), ΔE_D^{unocc} (eV), and ΔE_L^{unocc} (eV) represent the spin splitting at *D* valley for the highest occupied states, the lowest unoccupied states, and the spin splitting at *L* valley for the lowest unoccupied state, respectively, while $\alpha_{R,\Gamma}^{occ}$ (eVÅ) and $\alpha_{R,\Gamma}^{unocc}$ (eVÅ) show the Rashba parameters around the Γ point calculated for the highest occupied and lowest unoccupied states, respectively.

Termination systems	ΔE_D^{occ} (eV)	ΔE_D^{unocc} (eV)	ΔE_L^{unocc} (eV)	$\alpha_{R,\Gamma}^{occ}$ (eVÅ)	$\alpha_{R,\Gamma}^{unocc}$ (eVÅ)
Se-SrO	0.11	0.09	0.24	0.025	0.042
Se-TiO_2	0.0.08	0.04	0.11	0.028	0.032

IV. CONCLUSION

In summary, based on first-principles DFT calculations supported by symmetry analysis, we have systematically investigated the SOC-related properties of the strained Bi_2O_2Se ML. Breaking the crystal inversion symmetry of 2D Bi_2O_2Se ML with an external electric field causes the formation of Rashba-spin-valley states, characterized by Rashba-type spin splitting around the Γ valley and spin-valley coupling at D valleys along the $\Gamma - M$ line. In contrast to the Rashba-spin-valley states widely studied on previously reported 2D materials [10,14–18,26–32], we observed persistent spin texture with in-plane orientation around the D valleys, as well as conventional Rashba-type spin textures around the Γ valley. The electric field-induced reduction of crystal symmetry from D_{4h} to C_{4v} point group is responsible for these spin textures, which is confirmed by a $\vec{k} \cdot \vec{p}$ model derived from symmetry analysis. Importantly, manipulating the Rashba and spin-valley states through biaxial strain provides an effective route to control the spin textures and spin splitting, which prevents electron backscattering, and hence significantly enhances the efficiency of the spin transport.

Since the Rashba-spin-valley states observed in the present study are solely enforced by the C_{4v} point group symmetry, it is expected that these states can also be achieved on other 2D materials having a similar point group symmetry. Recently, another layered bismuth oxychalcogenide has been experimentally reported, including Bi_2O_2Te [75] and Bi_2O_2S [76], which possess a similar crystal symmetry. Therefore, similar features of the Rashba-spin-valley states could be observed.

Finally, the potential of utilizing the Bi_2O_2Se ML in spintronics and valleytronics-based devices is emphasized by considering a practical system, specifically the Bi_2O_2Se ML/$SrTiO_3$ (001) heterointerface. This system supports robust Rashba-spin-valley states, highlighting its relevance in realistic applications. Therefore, this prediction is expected to trigger further theoretical and experimental studies to clarify the emergence of the Rashba-spin-valley states in 2D-based bismuth oxychalcogenide systems, which would be useful for future spintronic and valleytronic applications.

ACKNOWLEDGMENTS

This work was supported by a collaborative research project (No. 101/UN1/FMIPA.1.3/KP/PT.01.03/2023) supported by the Faculty of Mathematics and Natural Sciences, Universitas Gadjah Mada, Indonesia. The computation in this research was performed using the computer facilities at Universitas Gadjah Mada, Indonesia.

[1] A. Manchon, H. C. Koo, J. Nitta, S. M. Frolov, and R. A. Duine, New perspectives for Rashba spin-orbit coupling, Nat. Mater. **14**, 871 (2015).

[2] J. R. Schaibley, H. Yu, G. Clark, P. Rivera, J. S. Ross, K. L. Seyler, W. Yao, and X. Xu, Valleytronics in 2D materials, Nat. Rev. Mater. **1**, 16055 (2016).

[3] E. C. Ahn, 2D materials for spintronic devices, npj 2D Mater. Appl. **4**, 17 (2020).

[4] E. I. Rashba, Properties of semiconductors with an extremum loop. 1. Cyclotron and combinational resonance in a magnetic field perpendicular to the plane of the loop, Sov. Phys. Solid State **2**, 1109 (1960) [Fiz. Tverd. Tela **2**, 1224 (1960)].

[5] G. Dresselhaus, Spin-orbit coupling effects in zinc blende structures, Phys. Rev. **100**, 580 (1955).

[6] D. Di Sante, P. Barone, R. Bertacco, and S. Picozzi, Electric control of the giant Rashba effect in bulk GeTe, Adv. Mater. **25**, 509 (2013).

[7] E. Plekhanov, P. Barone, D. Di Sante, and S. Picozzi, Engineering relativistic effects in ferroelectric SnTe, Phys. Rev. B **90**, 161108(R) (2014).

[8] S. Kuhlen, K. Schmalbuch, M. Hagedorn, P. Schlammes, M. Patt, M. Lepsa, G. Güntherodt, and B. Beschoten, Electric Field-Driven Coherent Spin Reorientation of Optically Generated Electron Spin Packets in InGaAs, Phys. Rev. Lett. **109**, 146603 (2012).

[9] S. Datta and B. Das, Electronic analog of the electro-optic modulator, Appl. Phys. Lett. **56**, 665 (1990).

[10] D. Xiao, G.-B. Liu, W. Feng, X. Xu, and W. Yao, Coupled Spin and Valley Physics in Monolayers of MoS_2 and Other Group-VI Dichalcogenides, Phys. Rev. Lett. **108**, 196802 (2012).

[11] H.-Z. Lu, W. Yao, D. Xiao, and S.-Q. Shen, Intervalley Scattering and Localization Behaviors of Spin-Valley Coupled Dirac Fermions, Phys. Rev. Lett. **110**, 016806 (2013).

[12] O. Gunawan, Y. P. Shkolnikov, K. Vakili, T. Gokmen, E. P. De Poortere, and M. Shayegan, Valley Susceptibility of an Interacting Two-Dimensional Electron System, Phys. Rev. Lett. **97**, 186404 (2006).

[13] A. Rycerz, J. Tworzydło, and C. W. J. Beenakker, Valley filter and valley valve in graphene, Nat. Phys. **3**, 172 (2007).

[14] K. F. Mak, K. L. McGill, J. Park, and P. L. McEuen, The valley Hall effect in MoS_2 transistors, Science **344**, 1489 (2014).

[15] M. Onga, Y. Zhang, T. Ideue, and Y. Iwasa, Exciton Hall effect in monolayer MoS_2, Nat. Mater. **16**, 1193 (2017).

[16] S. Sheoran, S. Monga, A. Phutela, and S. Bhattacharya, Coupled spin-valley, Rashba effect, and hidden spin polarization in WSi_2N_4 family, J. Phys. Chem. Lett. **14**, 1494 (2023).

[17] C. Yang, Z. Song, X. Sun, and J. Lu, Valley pseudospin in monolayer $MoSi_2N_4$ and $MoSi_2As_4$, Phys. Rev. B **103**, 035308 (2021).

[18] W. Zhou, L. Wu, A. Li, B. Zhang, and F. Ouyang, Structural symmetry, spin-orbit coupling, and valley-related properties of monolayer WSi_2N_4 family, J. Phys. Chem. Lett. **12**, 11622 (2021).

[19] H. Zeng, J. Dai, W. Yao, D. Xiao, and X. Cui, Valley polarization in MoS_2 monolayers by optical pumping, Nat. Nanotechnol. **7**, 490 (2012).

[20] T. Cao, G. Wang, W. Han, H. Ye, C. Zhu, J. Shi, Q. Niu, P. Tan, E. Wang, B. Liu, and J. Feng, Valley-selective circular dichroism of monolayer molybdenum disulphide, Nat. Commun. **3**, 887 (2012).

[21] R. Wakatsuki, Y. Saito, S. Hoshino, Y. M. Itahashi, T. Ideue, M. Ezawa, Y. Iwasa, and N. Nagaosa, Nonreciprocal charge transport in noncentrosymmetric superconductors, Sci. Adv. **3**, e1602390 (2017).

[22] M. I. Dyakonov and V. I. Perel, Spin relaxation of conduction electrons in noncentrosymmetric semiconductors, Sov. Phys. Solid State **13**, 3023 (1972).

[23] Y. Araki, G. Khalsa, and A. H. MacDonald, Weak localization, spin relaxation, and spin diffusion: Crossover between weak and strong Rashba coupling limits, Phys. Rev. B **90**, 125309 (2014).

[24] H. Liu, J. Chen, H. Yu, F. Yang, L. Jiao, G.-B. Liu, W. Ho, C. Gao, J. Jia, W. Yao, and M. Xie, Observation of intervalley quantum interference in epitaxial monolayer tungsten diselenide, Nat. Commun. **6**, 8180 (2015).

[25] L. Yang, N. A. Sinitsyn, W. Chen, J. Yuan, J. Zhang, J. Lou, and S. Crooker, Long-lived nanosecond spin relaxation and spin coherence of electrons in monolayer MoS_2 and WS_2, Nat. Phys. **11**, 830 (2015).

[26] S.-B. Yu, M. Zhou, D. Zhang, and K. Chang, Spin Hall effect in the monolayer Janus compound Mosse enhanced by Rashba spin-orbit coupling, Phys. Rev. B **104**, 075435 (2021).

[27] M. A. U. Absor, H. Kotaka, F. Ishii, and M. Saito, Tunable spin splitting and spin lifetime in polar WsTe monolayer, Jpn. J. Appl. Phys. **57**, 04FP01 (2018).

[28] Q.-F. Yao, J. Cai, W.-Y. Tong, S.-J. Gong, J.-Q. Wang, X. Wan, C.-G. Duan, and J. H. Chu, Manipulation of the large Rashba spin splitting in polar two-dimensional transition-metal dichalcogenides, Phys. Rev. B **95**, 165401 (2017).

[29] A. Rezavand, N. Ghobadi, and B. Behnamghader, Electronic and spintronic properties of Janus $MSi_2P_xAs_y$ (M = Mo, W) monolayers, Phys. Rev. B **106**, 035417 (2022).

[30] G. Hussain, A. Samad, M. Ur Rehman, G. Cuono, and C. Autieri, Emergence of Rashba splitting and spin-valley properties in Janus $MoGeSiP_2As_2$ and $WGeSiP_2As_2$ monolayers, J. Magn. Magn. Mater. **563**, 169897 (2022).

[31] Y. Wang, W. Wei, H. Wang, N. Mao, F. Li, B. Huang, and Y. Dai, Janus Tixy monolayers with tunable berry curvature, J. Phys. Chem. Lett. **10**, 7426 (2019).

[32] R. Ahammed and A. De Sarkar, Valley spin polarization in two-dimensional h−MN(M = Nb, Ta) monolayers: Merger of valleytronics with spintronics, Phys. Rev. B **105**, 045426 (2022).

[33] F. Sheng, C. Hua, M. Cheng, J. Hu, X. Sun, Q. Tao, H. Lu, Y. Lu, M. Zhong, K. Watanabe, T. Taniguchi, Q. Xia, Z.-A. Xu, and Y. Zheng, Rashba valleys and quantum Hall states in few-layer black arsenic, Nature (London) **593**, 56 (2021).

[34] M. Meng, S. Huang, C. Tan, J. Wu, Y. Jing, H. Peng, and H. Q. Xu, Strong spin–orbit interaction and magnetotransport in semiconductor Bi_2O_2Se nanoplates, Nanoscale **10**, 2704 (2018).

[35] J. Gao, F. Lu, X. Liu, J. Deng, X. Zhang, Z. Sun, X. Liu, X. Shi, N. Wang, Y. Wu, W. Wang, and X. Ding, Detection and tuning of spin-orbit interactions on inclined-grown Bi_2O_2Se nanoplates, Appl. Phys. Lett. **120**, 013105 (2022).

[36] J. Wu, H. Yuan, M. Meng, C. Chen, Y. Sun, Z. Chen, W. Dang, C. Tan, Y. Liu, J. Yin, Y. Zhou, S. Huang, H. Q. Xu, Y. Cui, H. Y. Hwang, Z. Liu, Y. Chen, B. Yan, and H. Peng, High electron mobility and quantum oscillations in non-encapsulated ultrathin semiconducting Bi_2O_2Se, Nat. Nanotechnol. **12**, 530 (2017).

[37] J. Wu, C. Tan, Z. Tan, Y. Liu, J. Yin, W. Dang, M. Wang, and H. Peng, Controlled synthesis of high-mobility atomically thin bismuth oxyselenide crystals, Nano Lett. **17**, 3021 (2017).

[38] C. Chen, M. Wang, J. Wu, H. Fu, H. Yang, Z. Tian, T. Tu, H. Peng, Y. Sun, X. Xu, J. Jiang, N. B. M. Schröter, Y. Li, D. Pei, S. Liu, S. A. Ekahana, H. Yuan, J. Xue, G. Li, J. Jia, Z. Liu, B. Yan, H. Peng, and Y. Chen, Electronic structures and unusually robust bandgap in an ultrahigh-mobility layered oxide semiconductor, Bi_2O_2Se, Sci. Adv. **4**, eaat8355 (2018).

[39] K. Zhang, C. Hu, X. Kang, S. Wang, Y. Xi, and H. Liu, Synthesis and thermoelectric properties of Bi_2O_2Se nanosheets, Mater. Res. Bull. **48**, 3968 (2013).

[40] Y. Liang, Y. Chen, Y. Sun, S. Xu, J. Wu, C. Tan, X. Xu, H. Yuan, L. Yang, Y. Chen, P. Gao, J. Guo, and H. Peng, Molecular beam epitaxy and electronic structure of atomically thin oxyselenide films, Adv. Mater. **31**, 1901964 (2019).

[41] G. Theurich and N. A. Hill, Self-consistent treatment of spin-orbit coupling in solids using relativistic fully separable *ab initio* pseudopotentials, Phys. Rev. B **64**, 073106 (2001).

[42] T. Ozaki, Variationally optimized atomic orbitals for large-scale electronic structures, Phys. Rev. B **67**, 155108 (2003).

[43] T. Ozaki and H. Kino, Numerical atomic basis orbitals from H to Kr, Phys. Rev. B **69**, 195113 (2004).

[44] T. Ozaki and H. Kino, Efficient projector expansion for the *ab initio* LCAO method, Phys. Rev. B **72**, 045121 (2005).

[45] J. P. Perdew, K. Burke, and M. Ernzerhof, Generalized Gradient Approximation Made Simple, Phys. Rev. Lett. **77**, 3865 (1996).

[46] W. Kohn and L. J. Sham, Self-consistent equations including exchange and correlation effects, Phys. Rev. **140**, A1133 (1965).

[47] K. Lejaeghere, G. Bihlmayer, T. Björkman, P. Blaha, S. Blügel, V. Blum, D. Caliste, I. E. Castelli, S. J. Clark, A. Dal Corso, S. de Gironcoli, T. Deutsch, J. K. Dewhurst, I. Di Marco, C. Draxl, M. Dułak, O. Eriksson, J. A. Flores-Livas, K. F. Garrity, L. Genovese, P. Giannozzi, M. Giantomassi, S. Goedecker, X. Gonze, O. Grånäs, E. K. U. Gross, A. Gulans, F. Gygi, D. R. Hamann, P. J. Hasnip, N. A. W. Holzwarth, D. Iuşan, D. B. Jochym, F. Jollet, D. Jones, G. Kresse, K. Koepernik, E. Küçükbenli, Y. O. Kvashnin, I. L. M. Locht, S. Lubeck, M. Marsman, N. Marzari, U. Nitzsche, L. Nordström, T. Ozaki, L. Paulatto, C. J. Pickard, W. Poelmans, M. I. J. Probert, K. Refson, M. Richter, G.-M. Rignanese, S. Saha, M. Scheffler, M. Schlipf, K. Schwarz, S. Sharma, F. Tavazza, P. Thunström, A. Tkatchenko, M. Torrent, D. Vanderbilt, M. J. van Setten, V. Van Speybroeck, J. M. Wills, J. R. Yates, G.-X. Zhang, and S. Cottenier, Reproducibility in density functional theory calculations of solids, Science **351**, aad3000 (2016).

[48] T. Tadano and S. Tsuneyuki, Self-consistent phonon calculations of lattice dynamical properties in cubic $SrTiO_3$ with first-principles anharmonic force constants, Phys. Rev. B **92**, 054301 (2015).

[49] H. Kotaka, F. Ishii, and M. Saito, Rashba effect on the structure of the Bi one-bilayer film: Fully relativistic first-principles calculation, Jpn. J. Appl. Phys. **52**, 035204 (2013).

[50] N. Yamaguchi and F. Ishii, Strain-induced large spin splitting and persistent spin helix at $LaAlO_3/SrTiO_3$ interface, Appl. Phys. Express **10**, 123003 (2017).

[51] Moh. Adhib Ulil Absor and F. Ishii, Large band splitting with tunable spin polarization in the two-dimensional ferroelectric

GaXY family (X = Se, Te; Y = Cl, Br, I), Phys. Rev. B **103**, 045119 (2021).

[52] S. A. Sasmito, M. Anshory, I. Jihad, and Moh. Adhib Ulil Absor, Reversible spin textures with giant spin splitting in two-dimensional GaXY (X = Se, Te; Y = Cl, Br, I) compounds for a persistent spin helix, Phys. Rev. B **104**, 115145 (2021).

[53] Moh. Adib Ulil Absor and I. Santoso, Reversible canted persistent spin textures in two-dimensional ferroelectric bilayer WTe_2, J. Appl. Phys. **132**, 183906 (2022).

[54] Moh. Adib. Ulil. Absor, A. Lukmantoro, and I. Santoso, Full-zone persistent spin textures with giant spin splitting in two-dimensional group IV–V compounds, J. Phys.: Condens. Matter **34**, 445501 (2022).

[55] Moh. Adib. Ulil. Absor, Y. Faishal, M. Anshory, I. Santoso, Sholihun, Harsojo, and F. Ishii, Highly persistent spin textures with giant tunable spin splitting in the two-dimensional germanium monochalcogenides, J. Phys.: Condens. Matter **33**, 305501 (2021).

[56] Moh. Adhib Ulil Absor, I. Santoso, N. Yamaguchi, and F. Ishii, Spin splitting with persistent spin textures induced by the line defect in the 1t phase of monolayer transition metal dichalcogenides, Phys. Rev. B **101**, 155410 (2020).

[57] J. Liang, T. Tu, G. Chen, Y. Sun, R. Qiao, H. Ma, W. Yu, X. Zhou, C. Ma, P. Gao, H. Peng, K. Liu, and D. Yu, Unveiling the fine structural distortion of atomically thin Bi_2O_2Se by third-harmonic generation, Adv. Mater. **32**, 2002831 (2020).

[58] Y. Zhang, Q. Gao, X. Han, and Y. Peng, Mechanical flexibility and strain engineered-band structures of monolayer Bi_2O_2Se, Phys. E **116**, 113728 (2020).

[59] H. Tang, B. Shi, Y. Wang, C. Yang, S. Liu, Y. Li, R. Quhe, and J. Lu, Layer-Dependent Photoabsorption and Photovoltaic Effects in Two-Dimensional Bi_2O_2X (X = S, Se, and Te), Phys. Rev. Appl. **15**, 064037 (2021).

[60] N. Wang, M. Li, H. Xiao, H. Gong, Z. Liu, X. Zu, and L. Qiao, Optimizing the thermoelectric transport properties of Bi_2O_2Se monolayer *via* biaxial strain, Phys. Chem. Chem. Phys. **21**, 15097 (2019).

[61] Z. Pang and T. Li, Mechanics and strain engineering of bulk and monolayer Bi_2O_2Se, J. Mech. Phys. Solids **157**, 104626 (2021).

[62] See Supplemental Material at http://link.aps.org/supplemental/10.1103/PhysRevB.108.035109 for the calculated results of phonon dispersion bands of the Bi_2O_2Se ML under the equilibrium conditions, the applied of biaxial strains, and external electric fields. The Supplemental Material also includes the stability and electronic structures of Bi_2O_2Se ML/$SrTiO_3$ [001].

[63] X.-P. Wang, X.-B. Li, N.-K. Chen, J.-H. Zhao, Q.-D. Chen, and H.-B. Sun, Electric field analyses on monolayer semiconductors: The example of InSe, Phys. Chem. Chem. Phys. **20**, 6945 (2018).

[64] X.-Q. Feng, H.-X. Lu, D.-N. Shi, J.-M. Jia, and C.-S. Wang, Semiconductor-metal transition induced by combined electric field and external strain in bilayer phosphorene, Solid State Commun. **337**, 114434 (2021).

[65] J. Schliemann, J. C. Egues, and D. Loss, Nonballistic Spin-Field-Effect Transistor, Phys. Rev. Lett. **90**, 146801 (2003).

[66] L. L. Tao and E. Y. Tsymbal, Persistent spin texture enforced by symmetry, Nat. Commun. **9**, 2763 (2018).

[67] C. Autieri, P. Barone, J. Sławińska, and S. Picozzi, Persistent spin helix in Rashba-Dresselhaus ferroelectric $CsBiNb_2O_7$, Phys. Rev. Mater. **3**, 084416 (2019).

[68] B. A. Bernevig, J. Orenstein, and S.-C. Zhang, Exact SU(2) Symmetry and Persistent Spin Helix in a Spin-Orbit Coupled System, Phys. Rev. Lett. **97**, 236601 (2006).

[69] P. Altmann, M. P. Walser, C. Reichl, W. Wegscheider, and G. Salis, Suppressed decay of a laterally confined persistent spin helix, Phys. Rev. B **90**, 201306(R) (2014).

[70] R. Winkler, S. Papadakis, E. De Poortere, and M. Shayegan, *Spin-Orbit Coupling in Two-Dimensional Electron and Hole Systems* (Springer, Berlin, 2003).

[71] S. Vajna, E. Simon, A. Szilva, K. Palotas, B. Ujfalussy, and L. Szunyogh, Higher-order contributions to the Rashba-Bychkov effect with application to the Bi/Ag(111) surface alloy, Phys. Rev. B **85**, 075404 (2012).

[72] R. Arras, J. Gosteau, H. J. Zhao, C. Paillard, Y. Yang, and L. Bellaiche, Rashba-like spin-orbit and strain effects in tetragonal $PbTiO_3$, Phys. Rev. B **100**, 174415 (2019).

[73] M. Anshory and M. A. U. Absor, Strain-controlled spin-splitting in the persistent spin helix state of two-dimensional snse monolayer, Phys. E **124**, 114372 (2020).

[74] L. C. Gomes and A. Carvalho, Phosphorene analogues: Isoelectronic two-dimensional group-IV monochalcogenides with orthorhombic structure, Phys. Rev. B **92**, 085406 (2015).

[75] W. Ai, J. Chen, X. Dong, Z. Gao, Y. He, Z. Liu, H. Fu, F. Luo, and J. Wu, High mobility and quantum oscillations in semiconducting Bi_2O_2Te nanosheets grown by chemical vapor deposition, Nano Lett. **22**, 7659 (2022).

[76] X. Yang, L. Qu, F. Gao, Y. Hu, H. Yu, Y. Wang, M. Cui, Y. Zhang, Z. Fu, Y. Huang, W. Feng, B. Li, and P. Hu, High-performance broadband photoelectrochemical photodetectors based on ultrathin Bi_2O_2S nanosheets, ACS Appl. Mater. Interfaces **14**, 7175 (2022).